 doi:10.20944/preprints202102.0603.v1

Article

Highly Graphitized Fe-N-C electrocatalysts prepared from chitosan hydrogel frameworks

Giorgia Daniel[1], Tomasz Kosmala[1], Federico Brombin[1], Marco Mazzucato[1], Alessandro Facchin[1], Maria Chiara Dalconi[2], Denis Badocco[1], Paolo Pastore,[1] Gaetano Granozzi[1] and Christian Durante[1,*]

1 Department of Chemical Sciences, University of Padova, Via Marzolo 1, 35131 Padova, Italy;
2 Department of Geoscience, University of Padova, via Gradenigo 6, 35131, Padova, Italy
* Correspondence: christian.durante@unipd.it, Tel.: +39-049-8275112

Abstract: The development of platinum group metal-free (PGM-free) electrocatalysts derived from cheap and environmentally friendly biomasses for oxygen reduction reaction (ORR) is a topic of relevant interest, particularly from the point of view of sustainability. Fe-nitrogen-doped carbon materials (Fe-N-C) have attracted particular interest as alternative to Pt-based materials, due to the high activity and selectivity of Fe-N_x active sites, the high availability and good tolerance to poisoning. Recently, many studies focused on developing synthetic strategies, which could transform N-containing biomasses into N-doped carbons. In this paper chitosan was employed as a suitable N-containing biomass for preparing Fe-N-C catalyst in virtue of its high N content (7.1%) and unique chemical structure. Moreover, the major application of chitosan is based on its ability to strongly coordinate metal ions, a precondition for the formation of Fe-N_x active sites. The synthesis of Fe-N-C consists in a double step thermochemical conversion of a dried chitosan hydrogel. In acidic aqueous solution, the preparation of physical cross-linked hydrogel allows to obtain sophisticated organization, which assure an optimal mesoporosity before and after the pyrolysis. After the second thermal treatment at 900 °C, a highly graphitized material was obtained, which has been fully characterized in term of textural, morphological and chemical properties. RRDE technique was used for understanding the activity and the selectivity of the material versus the ORR in 0.5 M H_2SO_4 electrolyte. Special attention was put in the determination of the active site density according to nitrite electrochemical reduction measurements. It was clearly established that the catalytic activity expressed as half wave potential linearly scales with the number of Fe-N_x sites. It was also established that the addition of the iron precursor after the first pyrolysis step leads to an increased activity because of both an increased number of active sites and of a hierarchical structure, which improves the access to active sites. At the same time, the increased graphitization degree, and a reduced density of pyrrolic nitrogen groups are helpful to increase the selectivity toward the $4e^-$ ORR pathway.

Keywords: ORR; PGM-free; iron; chitosan; biomass, acid electrolyte; iron-nitrogen-doped carbon; graphitization, site density, Fe-N_x

1. Introduction

The two main classes of materials that are currently explored for reaching the goal of expanding the market of Fuel Cells by addressing the goal of having an efficient and sustainable oxygen reduction reaction (ORR) at the cathodic electrode are low-content Pt or Platinum Group Metals (PGM)-free electrocatalysts [1]. The former group aims at producing highly active and durable (particle stability and poisoning resistance) electrocatalysts by reducing the Pt amount while maintaing its working life. Different approaches have been adopted, e.g. creation of Pt alloys with transition [2,3] or late earth metals [4–7] and/or by engineering of nanoparticles (NPs) size and shape [8,9], focusing also on the interaction with the support, usually undoped or heteroatom doped carbons [10–12]. The latter PGM-free route aims at finding materials with good activity and durability based on cheap and earth-abundant metals. Within the PGM-free group, the single site metal-

Preprints (www.preprints.org) | NOT PEER-REVIEWED | Posted: 26 February 2021 doi:10.20944/preprints202102.0603.v1

nitrogen-doped carbon (M-N-C) materials have emerged as the most promising candidate due to the low cost and their performances, which are slowly approaching those of Pt-based materials [13–17], in particular in alkaline environment. Among all M-N-C materials, Fe-N-C has become the most studied and promising system due to the good activity and stability if compared with other metals like Co, Mn, or Zn [18]. However, the nature of the active sites in these catalysts is still under debate; in addition, the role of the support, of the doping precursor and of the synthesis condition in term of activity and type of sites formed still has to be fully rationalized [19,20]. In this context, the development of PGM-free electrocatalysts for ORR derived from cheap and highly available precursors is a topic of relevant interest, which could have a relevant impact on the future market offuel cells [16,21], metal air batteries [22,23] and electrochemical sensors for O_2 detection [24,25]. For this reason, great efforts have been and continue to be made for exploring the use of cheap and abundant biomasses [26,27] as a feedstock to obtain new materials with improved activity [28], selectivity [29,30] and stability [31,32].

Hierarchical mesoporous carbons (MC) are the most interesting materials for application in electrocatalysis; in fact, while micropores favors the hosting of M-N_x active sites [33,34], mesopores play a pivotal role in conveying the reagents to the active sites. Without mesopores, a large part of physical surface area is not reached by reactants because the diffusion is hindered [35]. The distribution and shape of pores are fundamental to tune and improve catalytic performance. Furthermore, the presence of different heteroatom functional groups embedded on a 3D hierarchical porous structure and the graphitization degree can induce higher catalytic performance and stability, respectively [36]. To control textural and porous structure of MCs, the use of inorganic templates (hard template approach) [10,37–41], or self-assembled nanostructure of organic molecules (soft template approach) [42,43] can be exploited. In the latter method, the chemical interactions between the template and the carbon precursor rule the success of the templating. These two methods have demonstrated to be most successful for the synthesis of a well-ordered and uniform pore structure. A third way is the self-templating approach where specific etching molecules, e.g. CO_2, CO, SO_2, NH_3, or particles, e.g. metal, metal oxides or carbides, are generated *in situ* and are able to induce the formation of micropores [10] or mesopores [44].

In the last years, the conversion of biomasses [27,45–52] or waste polymers [44] into activated carbon has become a promising approach for the synthesis of self-templating M-N-C catalysts. In this paper we present the synthesis and characterization of Fe-N_x doped MCs by thermochemical conversion of a preconditioned hydrogel, prepared from a refined biomass, i.e. chitosan, without the use of any additional template or carbon black support. Chitosan is a polysaccharide obtained from the deacetylation of chitin which is easily extracted from shrimp's shell [53]. Chitosan is biocompatible and was proved to be a useful materials in a wide range of fields, such as food industry, water treatment [54], tissue engineering, medical area [55], supercapacitor [56] ,CO_2 hydrogenation [57], reduction of nitro compounds [58], batteries [59,60] and fuel cell devices [32,61,62]. Furthermore, chitosan is a suitable N-containing biopolymeric material with a high N content (7.1%) and jellify producing a self-template hydrogel precursor. The hydrogel reduces the aggregation ensuring an effectively homogenous heteroatom doping, while its 3D porous architecture can be preserved or even improved in the final catalyst. The chitosan derived MC was employed as platform for the pinning of Fe-N_x sites and the final electrocatalysts performance for ORR was rationalized according to the textural and physico-chemical properties of the Fe-N-C materials.

2. Results and Discussion

The synthesis of chitosan-derived Fe-N-C catalysts is based on the preliminary gelation of chitosan followed by the synthetic protocol explained in detail in the paragraph 3.1 and sketched in Scheme 1. Chitosan is the main source of carbon and nitrogen, 1,10 phenan-

Preprints (www.preprints.org) | NOT PEER-REVIEWED | Posted: 26 February 2021 doi:10.20944/preprints202102.0603.v1

throline is used as an auxiliary nitrogen source, whereas $FeCl_2$, $FeCl_3$ or tris(1,10-phenanthroline)iron(II)-chloride ($Fe(Phen)_3Cl_2$) were employed as alternative iron precursors for the Fe-N_x formation. The different precursors were mixed with chitosan or chitosan derived carbon at different stage during the preparation. Different final materials were obtained which are labelled as Fe-N-Cn (n=1-5). For the sake of clarity all the conditions employed for the preparation of the different Fe-N-Cn materials are resumed in

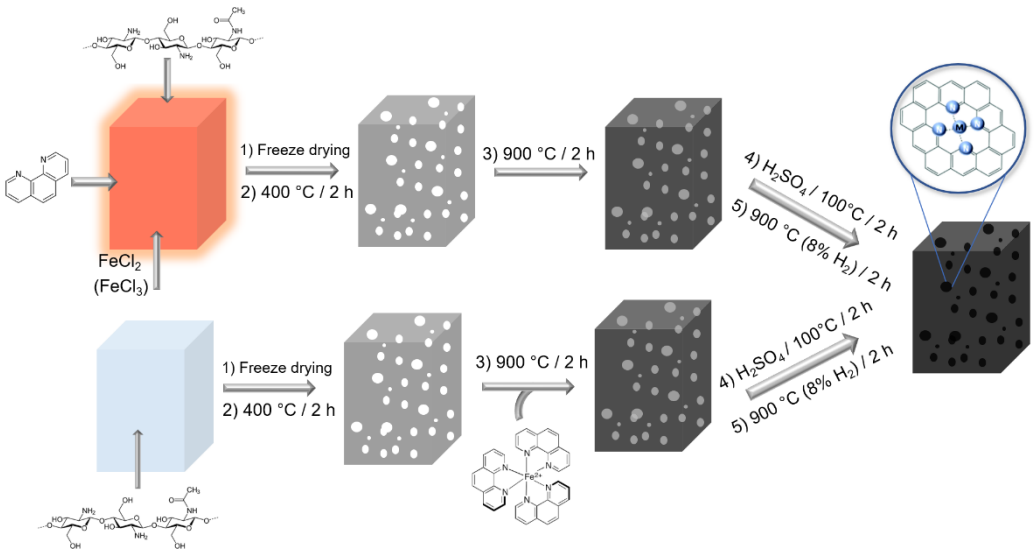

Scheme 1: Schematic representation of different steps for the synthesis of a chitosan-derived Fe-N-C electrocatalysts.

Table 1.

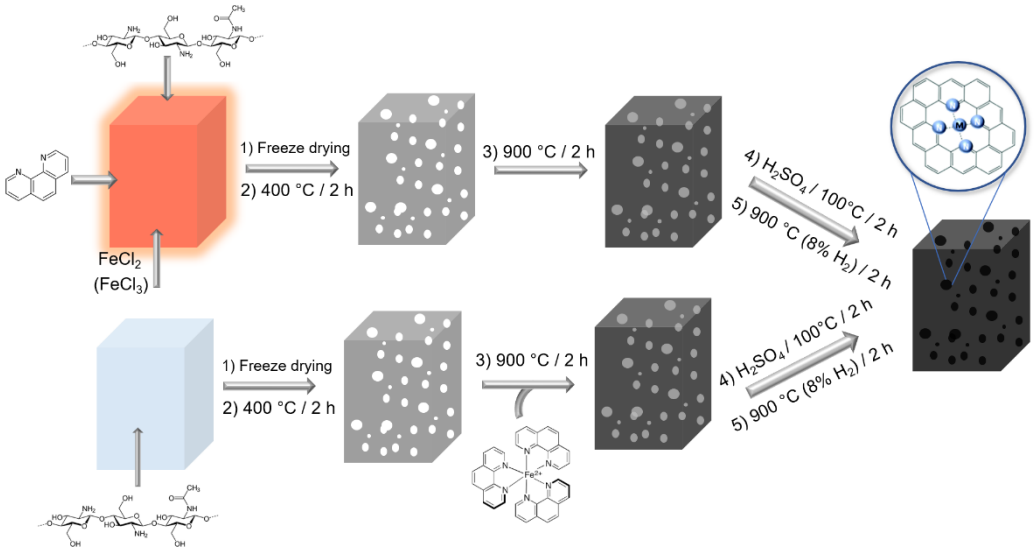

Scheme 1: Schematic representation of different steps for the synthesis of a chitosan-derived Fe-N-C electrocatalysts.

Table 1: Different synthetic conditions for chitosan-derived Fe-N-Cn (n=1-5) electrocatalysts.

Preprints (www.preprints.org) | NOT PEER-REVIEWED | Posted: 26 February 2021 doi:10.20944/preprints202102.0603.v1

Samples	*Precursors*					*Details*
	chitosan	Phen	$Fe^{(II)}Cl_2$	$Fe^{(III)}Cl_3$	$Fe(Phen)_3Cl_2$	Added after first pyrolysis at 400 °C
Fe-N-C1	✔	✔	✔			
Fe-N-C2	✔	✔		✔		
Fe-N-C3	✔		✔			
Fe-N-C4	✔		✔			✔
Fe-N-C5	✔				✔	✔

2.1. Morphological and textural properties

The morphology of the Fe-N-Cn catalysts was investigated by TEM (**Error! Reference source not found.**). All of them show a mixed structure of compact lamellae and *sponge-like* structures. Several Fe-based NPs are trapped within the structure as clearly visible by the different image contrast due to the higher electron density of Fe with respect to C. Some *alveoli like* pore can be recognized, whose size is equal to those of Fe-based NPs. This matching allows to suggest that the formed NPs act as a templating agent, which decompose or migrate to agglomerate in larger NPs during the pyrolysis leaving voids in the carbonaceous network. The high density of Fe-based NPs and the *alveoli like* pores could be explained by the mechanism proposed by Wang Y. *et al*. for magnetite production [63], where the complex between chitosan and iron becomes a magnetite Fe_3O_4 NP after alkaline treatment. There are no remarkable differences on the final structure when phenanthroline or different iron precursors are used. It is important to stress that the Fe-based NPs are enveloped in a carbon shell (Fe@C), so that they are partially protected against the acid treatment. In fact, comparing the images before and after acid wash (Figure S1), the NPs are not totally removed: as an example, the iron content in Fe-N-C3 is reduced from 15.2 wt.% to 4.9 wt.% (**Table 2**).

A completely different structure can be observed in Fe-N-C4 and Fe-N-C5 where $FeCl_2$ and $Fe(Phen)_3Cl_2$ were respectively added only after the first pyrolysis at 400 °C. In fact, compact carbon sheets are no longer present, whereas the sole sponge-like structure remains. Also, in this case the porous structure is due to the self-templating effect of Fe-based NPs. In this case, a much lower number of Fe@C NPs can be recognized contrary to Fe-N-Cn (n = 1-3). This can be justified by the fact that iron is added after the pre-formation of the carbon scaffold, which is no longer able to reorganize. Without being protected by a carbon shell, Fe-based NPs are more effectively removed by the acid leaching as demonstrated by ICP-MS results in **Table 2**, where the Fe content in Fe-N-Cn (n = 4,5) decreases below 1 % wt. after the acid wash.

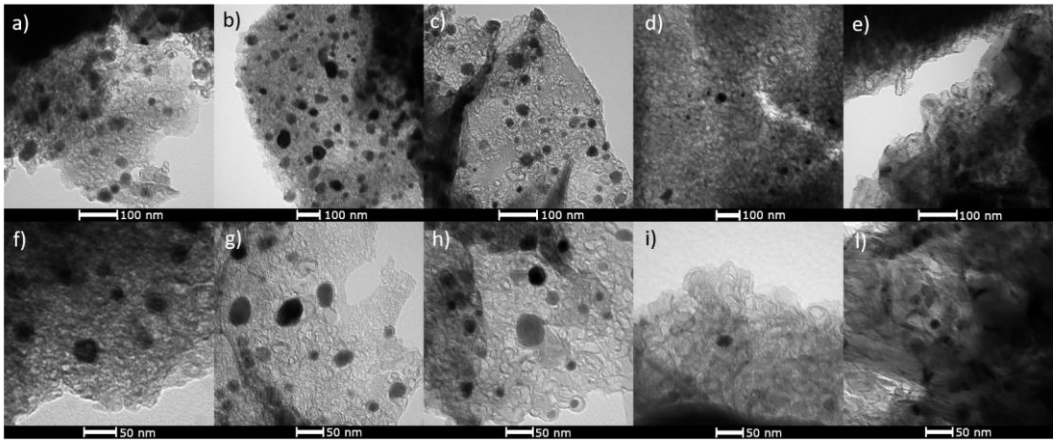

Figure 1 TEM images of (a,f) Fe-N-C1; (b,g) Fe-N-C2; (c,h) Fe-N-C3; (d,i) Fe-N-C4 and (e,l) Fe-N-C5

Preprints (www.preprints.org) | NOT PEER-REVIEWED | Posted: 26 February 2021 doi:10.20944/preprints202102.0603.v1

The porous structure was further characterized by N_2 ads/desorption and the results are reported in **Figure 2** and **Table 2**. Fe-N-C1 has a very high surface area (627 $m^2\ g^{-1}$) thanks to the high density of micro and mesopores, whose formation seems to be encouraged by 1,10-phenanthroline [41]. The hysteresis of Fe-N-C1 is a H5-like type, which is typical of certain pore structures with both open and blocked mesopores [64]. The desorption branch presents a rapid step-down at 0.45 p/p^0, i.e. the cavitation pressure, which is due to ink-bottle shape pores. For this reason, these isotherms are analyzed applying cylindrical/spherical QSDFT adsorption model [65]. Fe-N-C2 and Fe-N-C3 present the same IV(a) type isotherm and the same H4 hysteresis, typical of micro-mesoporous materials. In fact, their mesoporosity is similar, the main difference being in the uptake at low p/p^0 due to microporosity, clearly visible in **Figure 2**a: Fe-N-C2 and Fe-N-C3 have a different microporous surface of 157 $m^2\ g^{-1}$ and 248 $m^2\ g^{-1}$, respectively, while they have the same pore size distribution as reported in **Figure 2**b. The textural properties appear to be not affected by the addition of iron after the first pyrolysis. In fact, Fe-N-C3 and Fe-N-C4 have the same isotherms and similar textural properties (see **Table 2**). The isotherm for Fe-N-C5 is a mixture of II and IV(a) types, due to the presence of both macropores and mesopores and the hysteresis is a mixed H2(a)/H3 type. This type of isotherm is given by a heterogeneous pore network with macropores (H3 type), and mesopores (H2 type). The steeper desorption branch at 0.45 p/p^0, which identifies H2(a) hysteresis, is due to pore-blocking in a narrow range of pore necks.

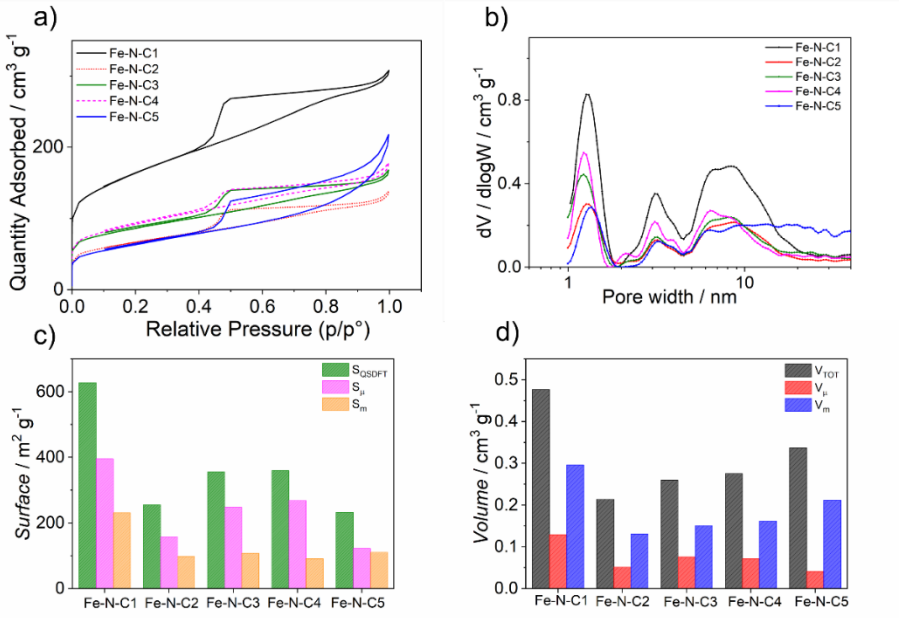

Figure 2 (a) N_2 adsorption/desorption isotherms and (b) pore size distribution of the investigated catalysts. Micro-, meso- and total (c) surface area and (d) pore volume.

The pore size is similar in all the samples, except for the higher density of pores with size > 10 nm in Fe-N-C5 (**Figure 2**b). **Figure 2**c and d report the comparison of surface area and volume of micropores and mesopores: all the sample have important components of both micropores and mesopores even though to a different extent. Accessibility and connectivity among pores are fundamental parameters for the heterogeneous catalysis. For this reason, a hierarchical factor (HF) can be calculated as

$$HF = \frac{V_\mu}{V_{TOT}} \cdot \frac{S_m}{S_{QSDFT}} \quad (1)$$

Preprints (www.preprints.org) | NOT PEER-REVIEWED | Posted: 26 February 2021 doi:10.20944/preprints202102.0603.v1

were V_μ and V_{TOT} are the volume of micropore and the total volume pore respectively, whereas S_m and S_{QSDFT} are the surface area of mesopore and the total surface area determined by the quenched-solid density-functional-theory model, which considers the adsorbant as a hardcore sphere interacting with fluid molecules. The HF is generally used to evaluate the catalytic activity of zeolite, but the general applicability has been recently challenged [66]. In the best catalysts should maximize the HF factor by comprising the enhancement of the mesopore surface area without a severe penalization of the micropore volume aiming at improving the reagent and product transport efficiency to the active site. If we take zeolites as reference materials, mostly microporous standard samples have moderate HF< 0.1, whereas those mostly mesoporous have HF < 0.05. Materials displaying high relative microporosity and low relative mesoporosity, have HF > 0.10, whereas system with spread hierarchical pores have HF > 0.15. Our Fe-N-Cn catalysts show HF values close to 0.1 or below attesting to be highly microporous with a moderate content of mesopores, that is promising for electrocatalytic applications since Fe-N_x sites are expected to form inside the micropores, whereas mesopores are useful to increase the accessibility to the active sites. Based on their HF values, the samples are rather similar from the structural point of view: the micro- and meso-porosity are balanced in the same way for all catalysts. In Fe-N-Cn (n = 4,5) the HF value is slightly lower than in Fe-N-Cn (n = 1-3) but this is principally due to a decrease of mesoporosity rather than an increase of microporosity (**Table 2**).

Table 2: Physical and chemical properties of some chitosan-based Fe-N-Cn electrocatalysts.

Supports					***N_2 ads/desorption isotherm***					
	C [a]	**N** [a]	**Fe** [b]		**S_{QSDFT}**	**V_{TOT}**	**V_{QSDFT}**	**S_μ**	**S_m**	**HF**
	%	%[a]	%[b]		m^2g^{-1}	$cm^3\,g^{-1}$	cm^3g^{-1}	m^2g^{-1}	$m^2\,g^{-1}$	
Fe-N-C1	86.78	0.44	n.a.	n.a.	627	0.477	0.425	396	232	0.10
Fe-N-C2	85.57	0.56	n.a.	n.a.	255	0.214	0.182	157	98	0.09
Fe-N-C3	81.71	0.68	15.2[c]	4.9[d]	356	0.260	0.224	248	108	0.09
Fe-N-C4	85.71	0.90	10.0[c]	0.6[d]	360	0.275	0.233	268	91	0.07
Fe-N-C5	89.25	0.45	9.6[c]	0.4[d]	233	0.337	0.253	122	111	0.06

[a] from elemental analysis, [b] ICP-MS, [c] before acid washing; [d] after acid washing

2.2. Chemical and spectroscopic characterization

Raman characterization was also performed on all samples, since it can give interesting insights on the degree of graphitization, size of graphite crystallites (L_a) and content of amorphous carbon (**Figure 3**). The spectra were deconvoluted with 4 (D4, D1, D3 and G) or 5 (D2) bands (Figure S3) in the region between 1100 and 1700 cm^{-1} [67,68] after a normalization relative to the G band peak (namely to the Raman shift around 1600 cm^{-1}). In the region between 2200 and 3200 cm^{-1}, 2 or 3 bands (2D4, 2D1and D1+G) were used to deconvolute the spectrum according to Sadezky et al. [68]. This spectral region is generally called the graphene/graphene oxide region because at least two distinct bands similar to those of graphene oxide are observed in materials such as Fe-N-C5 (**Figure 3**b).

All the catalysts have similar I_{D1}/I_G value ranging between 1.1 and 1.3 (Table S1), which classify these materials as nanocrystalline graphite according to Ferrari et al. [67] (**Figure 3**c). The size of carbon crystallites (L_a) can be calculated using the Tunista and Koenig equation:

$$\frac{I_{D1}}{I_G} = \frac{C_\lambda}{L_a} \quad (2)$$

where $C_\lambda = -126\ \text{Å} + \lambda_L * 0.033$. L_a ranges between 3 – 5 nm (**Figure 3**c) and finds its maximum value in Fe-N-C5, which shows an increased graphitization degree with respect the other catalysts. Fe-N-C5 presents four main changing features: (i) the G band is

Preprints (www.preprints.org) | NOT PEER-REVIEWED | Posted: 26 February 2021 doi:10.20944/preprints202102.0603.v1

more intense than D1 band, (ii) G band is split into two bands (G and D2), (iii) D3 area, which accounts for amorphous carbon is much lower than D3 in the other sample, and (iv) the second order bands are well defined. In particular, the 2D1 band, which is indicative of the ordered stacking of the graphene layers along the hexagonal axis in short or medium ranges, is very intense and sharp (**Figure 3**d) [69]. It is well evident that the employment of the $Fe(Phen)_2Cl_2$ complex after the first pyrolysis leads to a more graphitized carbon catalyst as confirmed also by the I_{D1}/I_G value, the lowest one, and also by the small D3 band area associated to amorphous carbon (Table S1 and **Figure 3**d). The higher graphitization of Fe-N-C5 is confirmed also by adopting the parameter R2 introduced by Beyssac et al. [70] and that can be calculated according to equation 3

$$R2 = \frac{I_{D1}}{I_G + I_{D1} + I_{D2}} \quad (3)$$

R2 value reflects the number of structural defects and assume value higher than 0.5 for poorly organized structure and lower than 0.5 for well-organized one. R2 is equal to 0.45 for Fe-N-C5, whereas is > 0.5 in all the other synthetized catalysts.

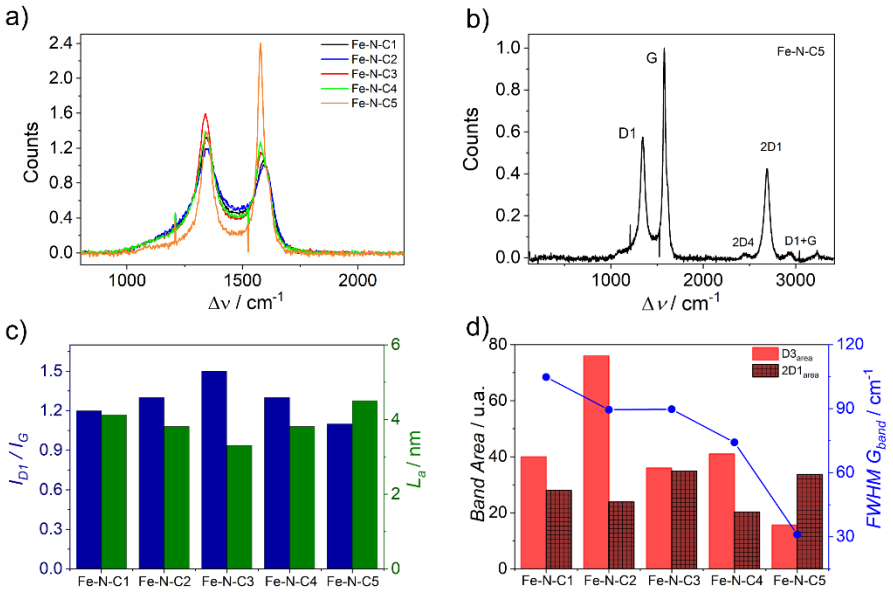

Figure 3 a) Overlay of spectra acquired in different synthetic condition, b) full range Raman spectrum for Fe-N-C5, c) I_{D1}/I_G ratio and L_a variation within the set of Fe-N-C catalysts, d) D3 and D2 band area and G band FWHM within the set of Fe-N-C catalysts.

The XRD analysis was performed on samples before acid washing, since otherwise the concentration of iron phases was too low to yield a clearly detectable diffraction signal (**Figure 4**a). The Fe-N-CX samples are composed of the following crystalline phases: graphite (C), metallic iron (α-Fe) and iron carbide (Fe_3C), but the content is different among different samples. Magnetite (Fe_3O_4) was detected only in Fe-N-C5. From a qualitatively evaluation of the diffraction patterns, the Bragg reflection at 30.4 °2θ from C (002) lattice planes is sharper for Fe-N-C5, which means a higher degree of crystallinity. The same conclusion was previously found from Raman spectroscopy analysis. A quantitative description of the peak broadening of graphite 002 reflection was achieved by profile fitting with an asymmetric (split width) Pseudo Voigt function. When iron is added after the first pyrolysis, the total width is reduced from 6.6 °2θ in Fe-N-C3 to 5.0 in Fe-N-C4 and the integrated intensity increases, becoming two times higher than in Fe-N-C3. The same consideration stands for Fe-N-C5. The 002 reflection intensity increment means that the stacking of graphite layers is not interrupted by amorphous carbon. For the other phases, which exhibited more defined reflections, a Williamson-Hall (W-H) plot analysis was tentatively applied. In Figure S4 the W-H plots of Fe_3O_4 and α-Fe are reported. The α-Fe showed two Bragg reflections in the measured 2θ range, thus the line profile analysis

Preprints (www.preprints.org) | NOT PEER-REVIEWED | Posted: 26 February 2021 doi:10.20944/preprints202102.0603.v1

was limited to two diffraction peaks, namely the 011 and 002 reflections. The integral breadth values, subtracted by the instrumental contribution, are reported in table x. The estimated mean crystallite size was derived by applying the Scherrer equation on each reflection, setting a shape factor K_β = 1. For sample Fe-N-C5, the sizes of α-Fe resulted equal to 49 nm for Bragg peak at 52.3 °2θ and 48 nm for Bragg peak at 77.2 °2θ (Table S2). The size of these particles is in general agreement with those obtained from TEM images, so that it is reasonable to assert that the most visible particles are principally made of metallic iron. The Fe_3O_4 phase displayed a more pronounced peak broadening (Figure S4) related to smaller crystallite sizes. As previously introduced, the acid washing removes the Fe_3O_4 and metallic particles, and the remaining ones are Fe_3C and a low percentage of α-Fe (Figure S5).

The composition of the exposed surface of Fe-N-Cn samples was investigated by a comprehensive XPS analysis, which evidenced the presence of iron, oxygen, carbon and nitrogen. The presence of the same elements was confirmed by ICP-MC (Fe) and elemental analysis (N and C) as reported in **Table 2**. It is interesting to underline that according to bulk elemental analysis, the use of 1,10-phenanthroline as an auxiliary nitrogen source does not bring any further increase of the nitrogen functional groups (**Table 2** and **Figure 4**c). Actually, the nitrogen content decreases from 0.68 wt.% (Fe-N-C3) to 0.44 wt.% (Fe-N-C1) when 1,10-phenanthroline is used. If $Fe(Phen)_3Cl_2$ is used as Fe^{3+} precursor, the nitrogen content increases up to 0.56 wt.%, and this was associated to the strong chelating effect exert by the trivalent cation. In fact, it seems that Fe^{3+} is more easily incorporated in the sample than Fe^{2+}. It seems then that the hydrogel acts as a carbon exchange resin, where the adsorption depends on pH and on chemical interaction. The maximum nitrogen surface content determined by XPS is limited to ca. 2 $\%_{wt.}$ (in Fe-N-C1 and Fe-N-C3, see Table S3). The N 1s peak was fitted with 6 components (**Figure 4**b) i.e. imine N (397.8 eV), pyridinic N (398.8 eV), Fe-N_x (399.9 eV), pyrrolic N (400.7 eV), graphitic N (401.7 eV) and N-O group (402.7 eV) [19,44]. Actually, the data show an apparent decrement of pyrrolic nitrogen and Fe-N_x, going from Fe-N-C1 to Fe-N-C5 (see **Figure 4**d and Table S3). The distribution of the N-functional groups appears to be influenced by the oxidation state of the iron precursor, as it can be observed from **Figure 4**d. In fact, the principal nitrogen groups which form when using Fe^{3+} are: N_x, pyrrolic and graphitic nitrogen, while using Fe^{2+} the imine and pyridinic groups may be singled out.

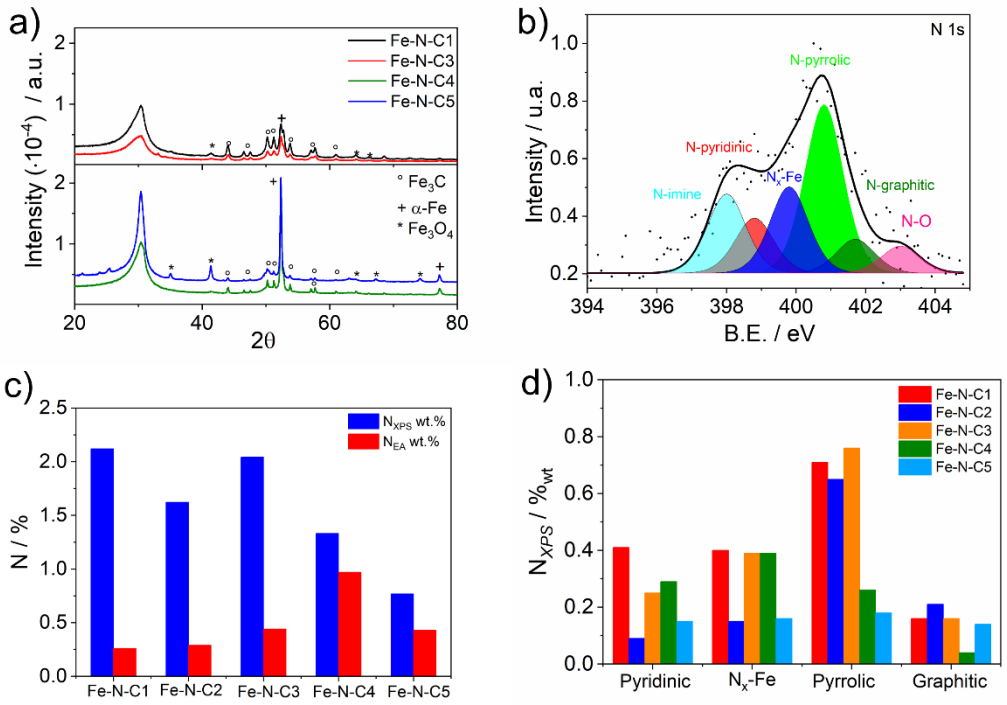

Preprints (www.preprints.org) | NOT PEER-REVIEWED | Posted: 26 February 2021 doi:10.20944/preprints202102.0603.v1

Figure 4 a) XRD spectra acquired before acid wash in H_2SO_4, b) example of high-resolution core-level XPS spectra of N 1s and deconvolution for Fe-N-C5; (c) superficial and bulk(N_{EA}) nitrogen content as determined by XPS and elemental analysis, respectively (d) surface nitrogen speciation in each Fe-N-Cn catalyst.

2.3. ORR electrochemical performace

The catalytic performance for oxygen reduction reaction was evaluated by using CV and LSV with RRDE. In **Figure 5**a we report a representative example of the voltammetric behavior of Fe-N-C5 in both Ar-purged and O_2-saturated 0.5 M H_2SO_4. In oxygen-saturated electrolyte, a very intense and narrow peak appears at around 0.75 V/RHE (scan rate at 2 mV s^{-1}) which is not present in the background and that can be convincedly assigned to the ORR process. All the other catalysts show very similar behavior, but with different E_p and I_p. **Figure 5**b reports the LSV curves for all the Fe-N-C catalysts. $E_{1/2}$ and j_k, representing the half wave potential and the kinetic current, respectively, are two objective descriptors of the catalytic process and it clearly appears that both shifts to more positive value passing from Fe-N-C1 to Fe-N-C5, attesting a superior catalytic activity for Fe-N-C5 (**Figure 5**c). The number of transferred electrons were calculated from the K-L plot and compared to the value determined by RRDE (**Figure 5**d). The two values are in fairly agreement attesting an almost 4 electron process at all the catalysts with a higher selectivity in those catalysts obtained with the post addition of iron precursors. The H_2O_2 yield ranges between 6% to 10 % reaching the lowest value in Fe-N-C5 (**Figure 5**d).

It is interesting to observe that H_2O_2 yield scale linearly with both: the percentage of pyrrolic functional groups determined by XPS analysis and the R2 parameter attesting the graphitization degree of the carbon material, i.e. the higher the $N_{pyrrolyc}$ density or the amorphous carbon fraction, the higher the χ_{H2O2} (**Figure 5**e and f).

The number of Fe-N_x sites was determined by the electrochemical nitrite stripping developed by Malko et al. [71,72]. This method is based on the selective interaction of Fe-N_x sites with probe molecule NO_2^-, which reversibly binds to the Fe center as nitrosyl at a buffered pH value of 5.2. The nitrosyl stripping charge, Q_{strip}, can be related to the gravimetric site density according to the formula:

$$\text{MSD [mol sites g}^{-1}] = \frac{Q_{strip}[C\ g^{-1}]}{n_{strip} F[C\ mol^{-1}]} \quad (4)$$

where n_{strip} is the number of electrons associated with the reduction of one adsorbed nitrosyl per site to NH_3. What we expect is to observe a variation of sites density depending on the synthetic procedure and therefore on the textural, morphological and chemical properties of the Fe-N-C catalysts. An example of the obtained electrochemical curves is reported in Figure S6a,b. The turnover frequency (TOF) of Fe-N_x sites is then given by the expression:

$$TOF[electron\ sites^{-1}\ s^{-1}] = \frac{j_K\ [A\ g^{-1}]}{MSD[mol\ sites\ g^{-1}] \cdot F[C\ mol^{-1}]} \quad (5)$$

where F is the Faraday constant, j_K is the kinetic current determined by the Tafel plot (Figure S6c) and MSD is the gravimetric active sites density. It becomes clear that the catalytic activity expressed as j_k is influenced either from a high turnover frequency or a high number of active sites (Figure S6d). It is interesting to observe that according to NO-stripping results (Table S4), the site density scale almost linearly (excluding the Fe-N-C1 point) with the half wave potentials of LSV recorded at different catalysts for the ORR process. This is a clear indication of how the catalytic activity depends on the number of Fe-N_x sites. Furthermore, the SD shows a good correlation also with the hierarchical factor HF, which is a descriptor of how much interconnected are micropores, where active sited should be located, and mesopores which favor the access to the active sites. The addition of iron precursor after the first pyrolysis step leads to an increased activity because of both: an increased number of active sites and to a hierarchical structure, which improve the access to those active sites. At the same time, the increased graphitization degree is helpful in increasing the selectivity because of a reduced density of pyrrolic nitrogen.

Preprints (www.preprints.org) | NOT PEER-REVIEWED | Posted: 26 February 2021 doi:10.20944/preprints202102.0603.v1

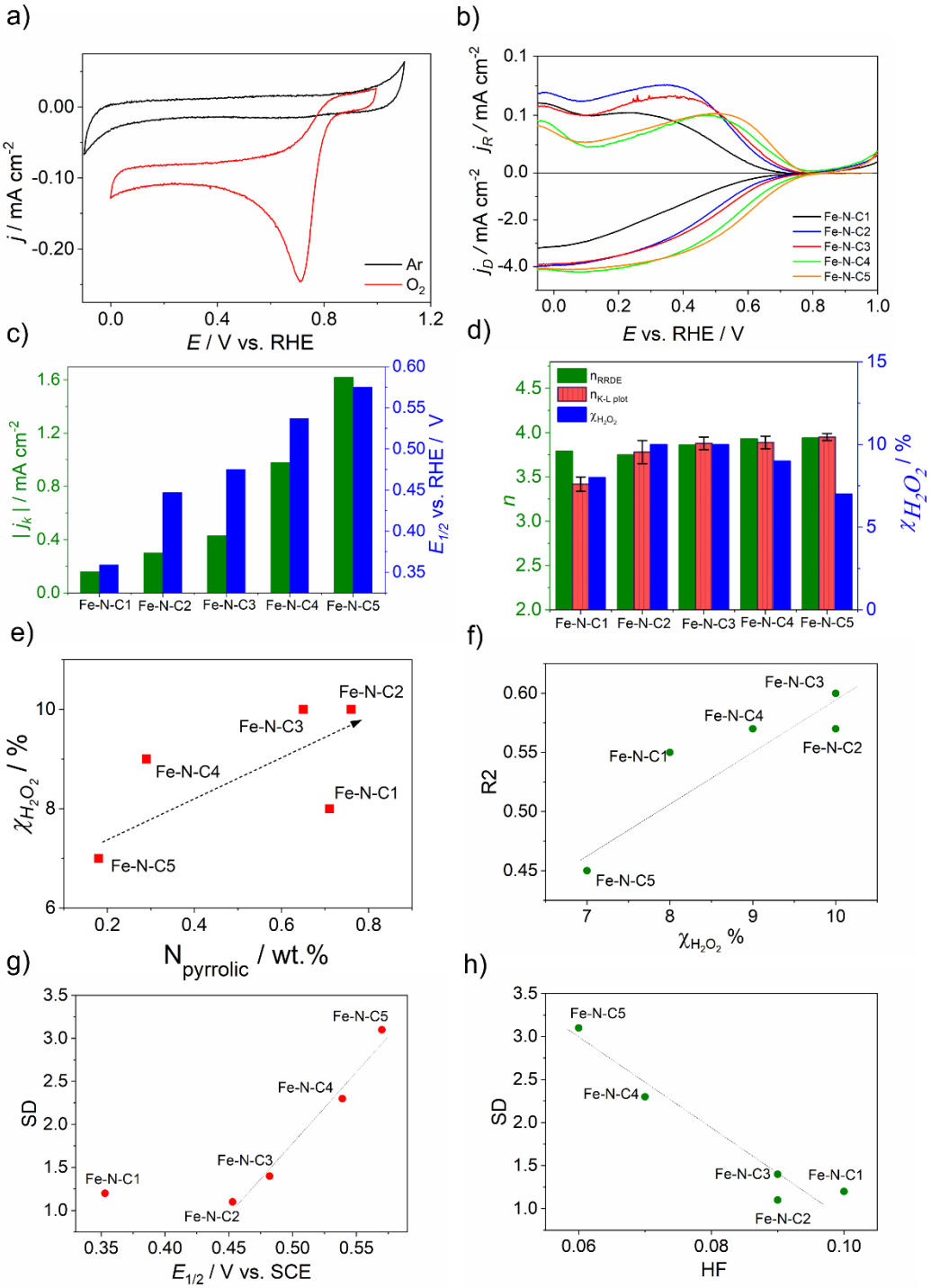

Figure 5 (a) cyclic voltammetry of Fe-N-C5 recorded in Ar purged and O_2-saturated 0.5 M H_2SO_4, v = 2 mV s^{-1} (b) LSV at RRDE recorded in O_2-saturated 0.5 M H_2SO_4, v = 2 mV s^{-1} and was ω =1600 rpm. (c) Kinetic current and half-wave potential for Fe-N-Cn; (d) number of transferred electron for ORR and H_2O_2 yield determined at 0.7 V_{RHE} for all the investigated catalysts; (e) correlation between the pyrrolic nitrogen species and H_2O_2 percentage ; (f) correlation between the graphitization parameter R2 calculated according to equation 3 and H_2O_2 percentage; (g) correlation between the site density determined by nitrosyl stripping and the half wave potential (h) correlation between the site density and the hierarchical factor HF determined by equation 1. In picture e-h, dotted lined are only intended for guiding the eye.

3. Materials and Methods

Preprints (www.preprints.org) | NOT PEER-REVIEWED | Posted: 26 February 2021 doi:10.20944/preprints202102.0603.v1

3.1 Synthesis of the catalysts.

The synthesis of chitosan-based Fe-N_x catalysts is based on the gelation of chitosan where chitosan is the main source of carbon and nitrogen, and 1,10-phenanthroline is used as an auxiliary nitrogen source. The iron doping is obtained using an inorganic salt such as $FeCl_2$, $FeCl_3$ or tris(1,10-phenanthroline)iron(II)-chloride ($Fe(Phen)_3Cl_2$). The synthesis consists in the formation of a chitosan hydrogel, followed by the removal of the solvent by freeze drying and the pyrolysis of the resulting material (Scheme 1). The hydrogel synthesis involved the dispersion of the chitosan powder (1.8 g) in an acetic acid solution (100 mL, 2 vol %), and the resulting mixture was vigorously stirred to ensure the complete solubilization. At acidic pH, the amine groups in the N-acetyl-β-(D)-glucosamine moiety are protonated to ammonium (pKa ($-NH_3^+$) = 6.3), favoring the solubilization of the polymer in water, thus obtaining a transparent, homogeneous and viscous solution. At this stage, 1,10-phenanthroline (Phen), $FeCl_2$ or $FeCl_3$ were used as secondary sources of nitrogen and as iron precursor, to induce the formation of Fe-N_x sites. The addition at this stage of Phen + $FeCl_2$, Phen + $FeCl_3$ or $FeCl_2$ leads to form Fe-N-Cn (X = 1-3) after the second pyrolysis (

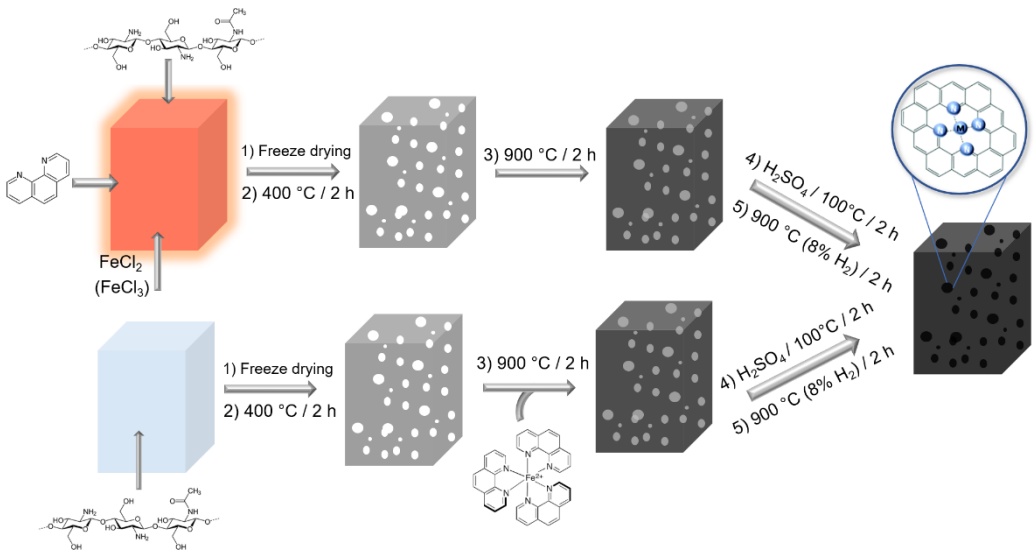

Scheme 1: Schematic representation of different steps for the synthesis of a chitosan-derived Fe-N-C electrocatalysts.

Table 1). The hydrogel formation occurred after pouring a 1 M NaOH solution to the chitosan solution. The gelation is not instantaneous but depends by the diffusion of OH^- through the chitosan solution. The obtained hydrogel was than rinsed with water until a neutral pH was reached and then cut into small pieces and afterward freeze-dried to remove all water. The dried gel was then thermally treated in a two-step pyrolysis procedure. The gel was heated in a Carbolite tubular furnace with a 75 sccm (standard cm^3/min) N_2 flux at 100 °C for 1 h, after which the temperature was raised up to 400 °C at a rate of 5 °C/min and kept at that temperature for 2 h. The resulting powder was ground by vibro-milling (Retsch MM 400, four steps of 4 min/10–25 Hz). As alternative to the addition of

Preprints (www.preprints.org) | NOT PEER-REVIEWED | Posted: 26 February 2021 doi:10.20944/preprints202102.0603.v1

nitrogen and iron precursor before the gelation process, $FeCl_2$ or tris(1,10-phenanthroline)iron(II)-chloride ($Fe(Phen)_3Cl_2$) were mixed after the first pyrolysis at 400°C to form Fe-N-C4 and Fe-N-C5, respectively after the second pyrolysis (

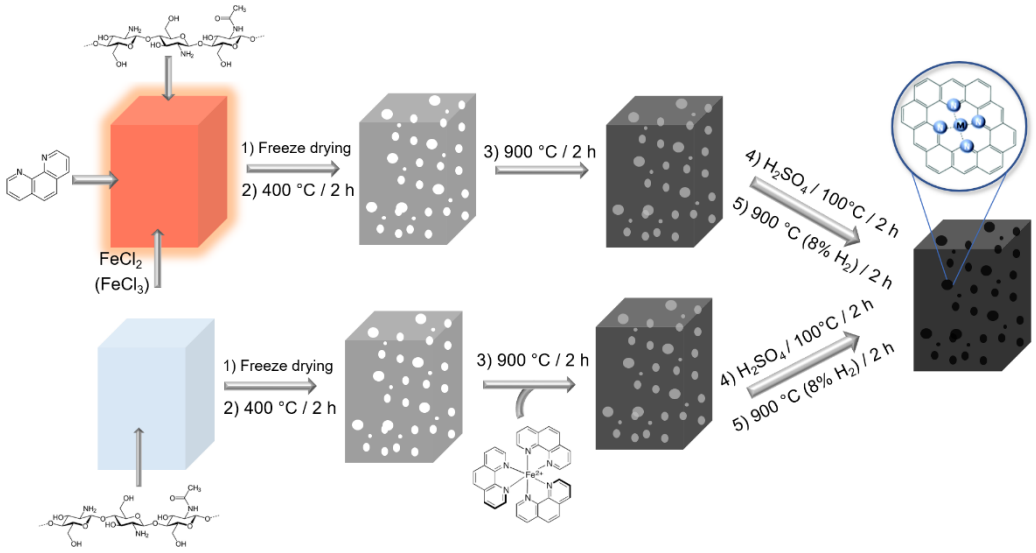

Scheme 1: Schematic representation of different steps for the synthesis of a chitosan-derived Fe-N-C electrocatalysts.

Table 1). Notwithstanding the timing in which chitosan, iron precursors and nitrogen auxiliary source are added, the mixture was re-pyrolyzed at 900 °C for 2 h under nitrogen atmosphere. The so obtained catalysts were acid washed in a 2 M H_2SO_4 solution, under reflux for 2h at 100 °C. After that, the solution is filtered, and the carbon is washed with milli-Q water several times and dried at 80 °C in oven for a night. Eventually, the Fe-N-C catalysts were activated at 900 °C for 2 h under a reducing atmosphere of (8 % H_2 in nitrogen), which is fluxed when 900 °C is reached. The final powder catalyst is grinded for 40 min at 22 Hz before the characterizations.

3.2 Electrochemical test

Cyclic voltammetry (CV) and linear sweep voltammetry (LSV) were carried out on a rotating ring-disc electrode (RRDE, Metrohm; d = 5 mm GC disk and a Pt ring), in both Ar-purged and O_2-saturated 0.5 M H_2SO_4 solution using an Autolab model 101N potentiostat. All measurements were done in a three-electrode cell thermostated at 25°C. The RRDE tip was used as working electrode, a graphite rod was used as counter-electrode and a homemade RHE as reference electrode. RHE consists in a spiral Pt wire settled to the closed end of a capillary glass tube filled with the electrolyte solution in which H_2 was directly electrogenerated at the Pt wire via chronoamperometric technique until half of the spiral was filled with gas.

The materials activity was investigated on a relatively thin catalyst layer loaded on GC surface via drop-casting after the preparation of an ink made approximately of a 8:2 mixture of water, an organic solvent (ethanol, isopropanol and THF) and Nafion (m_{nafion}/m_{cat} solution ≈ 0.8). To obtain a good dispersion the ink was sonicated both in a bath and probe sonicator. The loading was chosen to be 0.6 mg cm^{-2} as used in previous works [20,42].

All the materials were initially activated in Ar-purged electrolyte with extensive CV cycling at 200 mV s^{-1} until a stable current was observed. In ORR tests, O_2 was bubbled

Preprints (www.preprints.org) | NOT PEER-REVIEWED | Posted: 26 February 2021 doi:10.20944/preprints202102.0603.v1

inside the electrolyte solution for at least 30 min. The number of transferred electron (n) was determined by RRDE linear sweep voltammetry according to the following equation:

$$n = \frac{4|i_D|}{|i_D| + |i_R|/\mathrm{N}} \quad (6)$$

Where i_D is the current recorded at disk, i_R the current recorded at ring and N the collection efficiency, which is equal to 0.25 (determined by performing RRDE measurement in the presence of $K_4Fe(CN)_6$ in 0.5 M K_2SO_4 electrolyte). With the last analysis it is also possible to evaluate the percentage of hydrogen peroxide produced at the working electrode:

$$\chi_{H_2O_2}\% = 100 \cdot \frac{4-n}{2} = \frac{100 \cdot 2|i_R|}{N \cdot |i_D| + |i_R|} \quad (7)$$

Other parameters of interest are the half-wave potential ($E_{1/2}$), and the limiting current density (j_{lim}) determined from LSV analysis at 2 mV s^{-1} and 1600 rpm. The mass-transport corrected kinetic current density at a selected potential was calculated according to equation 8.

$$j_k = \frac{j_E \cdot j_{lim}}{j_E - j_{lim}} \quad (8)$$

where j_E is the current density at the selected potential E = 0.65 V vs RHE.

To evaluate the catalysts site density, nitrite (NO_2^-) poisoning and electrochemical stripping were performed following the procedure described by Malko et al. [71]. This procedure allows the selective poisoning of Fe-N_x site and the site density is determined by measuring the charge of NO reductive stripping during a CV measurement. The side density measurements were performed on a thin layer of catalyst deposited on a GC (RDE, Metrohm Ø = 5 mm) in a 0.5 M acetate buffer at pH 5.2. A loading of 0.2 mg cm^{-2} was chosen according to published procedure, the ink was let dry with the electrode in rotation at 130 rpm for about 20 min.

3.3 Physico-chemical characterization

X-ray photoemission spectroscopy (XPS) measurements were performed at room temperature in a UHV chamber (base pressure < $5 \cdot 10^{-9}$ mbar), equipped with a double anode X-ray source (Omicron DAR-400) and a hemispherical electron analyser (Omicron EIS-125). A non-monochromatized Mg-Kα radiation (hν=1253.6 eV) and pass energies of 50 eV and 20 eV for the survey and the single spectral windows, respectively, were used. The calibration of the Binding Energy (BE) scale was carried out using Au $4f_{7/2}$ as a reference (BE Au $4f_{7/2}$=84.0 eV). The XPS peak of nitrogen was deconvoluted into single components by using symmetrical Voigt functions.

XRD measurements were acquired by using a Panalytical X'Pert Pro diffractometer equipped with a Co anode X-ray tube (40 kV, 40 mA), Bragg–BrentanoHD optical module, and X'Celerator detector. Diffraction patterns were collected in the 5°-90° 2θ range with 2θ = 0.0338 ° virtual step size, counting an equivalent time of 300 s per step. The experimental patterns after some corrections are compared with the reference ones (Powder Diffraction File - PDF database) to individuate the possible phases. The main corrections concern the background and the instrumental broadening. In fact, in these samples, the background is bumped up by amorphous carbon matrix. The instrumental broadening was evaluated from the Bragg reflections of the reference standard LaB_6 (SRM 660c). The fitting profile was performed using a Pseudo-Voigt function, which allows to consider both Lorentzian and Gaussian broadening of the diffraction peaks, as demonstrated by the fitting of the graphite reflection of sample Fe-N-C3 in Figure S4.

Raman spectra were recorded using a micro-Raman set-up with a 1mW laser at 532 nm with 50xLWD objective (pinhole 25µm). N_2 adsorption/desorption isotherm were recorded at 77.3 K using an ASAP 2020 Plus instrument. Specific surface area of the samples was determined by BET analysis and with Quenched Solid Density Functional Theory (QSDFT) model, which showed to be more accurate compared to NLDFT, even if limited

 doi:10.20944/preprints202102.0603.v1

to pore dimension of 40 nm. In fact, it takes into account the roughness of the surface and chemical heterogeneity leading to a better fit of experimental data, in particular for disordered carbons. The total volume of pore was obtained applying Gurvitsch law at $p/p^0 \approx 0.98$. Elemental analysis (EA) was carried out using a Thermo Scientific Flash 2000 analyzer. Transmission electron microscopy (TEM) images were obtained with a FEI TECNAI G2 instrument operating at 100kV.5.

Inductively coupled plasma mass spectrometric analysis was performed with an Agilent Technologies 7700x ICP-MS. The samples (5 mg) were digested with 5 ml of 68% HNO_3 in a microwave system CEM EXPLORER SPD PLUS at a heating rate of 40 °C/min from room temperature to 220 °C (power of 300 W). The vial pressure was 400 psi and the digestion procedure took 15 minutes. Samples, after the digestion step, were suitably diluted and filtered before the ICP-MS measurement.

Conclusions

In this paper we consider the synthesis of Fe-N-C type catalysts by employing chitosan as sustainable carbon and nitrogen precursor. The synthetic procedure of Fe-N-C was refined and the optimal conditions for obtaining highly active and selective catalysts for oxygen reduction reaction consists in a double step thermochemical conversion of chitosan where an iron complex such as $Fe(Phen)_3Cl_2$ is added only after the first pyrolysis step. This leads to the formation of a catalysts with enhanced $Fe\text{-}N_x$ catalytic sites and a reduced amount of pyrrolic functional groups. The combined effects allow to increase the activity and the selectivity versus the $4e^-$ ORR. Furthermore, the Fe-N-C catalysts prepared according to this protocol shows a high graphitization degree, which help the selectivity versus the reduction of O_2 to H_2O and an optimal hierarchical pore structure, which enhances the accessibility to the $Fe\text{-}N_x$ active sites.

Supplementary Materials: The following are available online at www.mdpi.com/xxx/s1, Figure S1 to S5, Table S1 to S4.

Author Contributions: Conceptualization and methodology, C.D., G.D., M.M. and F.B.; formal analysis, investigation and data curation, G.D., F.B, T.K., D.B., P.P. and M.C. D.; writing—original draft preparation, C.D. A.F. and G.D.; writing—review and editing, C.D., A.F., M.M., and G.G.; supervision, C.D. All authors have read and agreed to the published version.

Funding: The research leading to these results has received funding from the Fuel Cells and Hydrogen 2 Joint Undertaking under grant agreement No 779366. This Joint Undertaking receives support from the European Union's Horizon 2020 research and innovation program, Hydrogen Europe and Hydrogen Europe Research.

Institutional Review Board Statement: "Not applicable"

Informed Consent Statement: "Not applicable"

Data Availability Statement: Data are available within the article.

Acknowledgments:

Conflicts of Interest: "The authors declare no conflict of interest."

References

1. Zhang, C.; Shen, X.; Pan, Y.; Peng, Z. A review of Pt-based electrocatalysts for oxygen reduction reaction. *Front. Energy* **2017**, *11*, 268–285, doi:10.1007/s11708-017-0466-6.
2. Stephens, I. E. L.; Bondarenko, A. S.; Grønbjerg, U.; Rossmeisl, J.; Chorkendorff, I. Understanding the electrocatalysis of oxygen reduction on platinum and its alloys. *Energy Environ. Sci.* **2012**, *5*, 6744–6762, doi:10.1039/c2ee03590a.
3. Wu, D.; Shen, X.; Pan, Y.; Yao, L.; Peng, Z. Platinum Alloy Catalysts for Oxygen Reduction Reaction: Advances, Challenges and Perspectives. *ChemNanoMat* **2020**, *6*, 32–41, doi:10.1002/cnma.201900319.
4. Zamburlini, E.; Jensen, K. D.; Stephens, I. E. L.; Chorkendorff, I.; Escudero-Escribano, M. Benchmarking Pt and Pt-lanthanide

sputtered thin films for oxygen electroreduction: fabrication and rotating disk electrode measurements. *Electrochim. Acta* **2017**, *247*, 708–721, doi:10.1016/j.electacta.2017.06.146.

5. Brown, R.; Vorokhta, M.; Khalakhan, I.; Dopita, M.; Vonderach, T.; Skála, T.; Lindahl, N.; Matolínová, I.; Grönbeck, H.; Neyman, K. M.; Matolín, V.; Wickman, B. Unraveling the Surface Chemistry and Structure in Highly Active Sputtered Pt_3Y Catalyst Films for the Oxygen Reduction Reaction. *ACS Appl. Mater. Interfaces* **2020**, *12*, 4454–4462, doi:10.1021/acsami.9b17817.
6. Brandiele, R.; Guadagnini, A.; Girardi, L.; Dražić, G.; Dalconi, M. C.; Rizzi, G. A.; Amendola, V.; Durante, C. Climbing the oxygen reduction reaction volcano plot with laser ablation synthesis of Pt_xY nanoalloys. *Catal. Sci. Technol.* **2020**, *10*, 4503–4508, doi:10.1039/D0CY00983K.
7. Brandiele, R.; Durante, C.; Grądzka, E.; Rizzi, G. A.; Zheng, J.; Badocco, D.; Centomo, P.; Pastore, P.; Granozzi, G.; Gennaro, A. One step forward to a scalable synthesis of platinum–yttrium alloy nanoparticles on mesoporous carbon for the oxygen reduction reaction. *J. Mater. Chem. A* **2016**, *4*, 12232–12240, doi:10.1039/C6TA04498K.
8. Meier, J. C.; Galeano, C.; Katsounaros, I.; Witte, J.; Bongard, H. J.; Topalov, A. A.; Baldizzone, C.; Mezzavilla, S.; Schüth, F.; Mayrhofer, K. J. J. Design criteria for stable Pt/C fuel cell catalysts. *Beilstein J. Nanotechnol.* **2014**, *5*, 44–67, doi:10.3762/bjnano.5.5.
9. Vidal-Iglesias, F. J.; Arán-Ais, R. M.; Solla-Gullón, J.; Herrero, E.; Feliu, J. M. Electrochemical Characterization of Shape-Controlled Pt Nanoparticles in Different Supporting Electrolytes. *ACS Catal.* **2012**, *2*, 901–910, doi:10.1021/cs200681x.
10. Brandiele, R.; Zerbetto, M.; Dalconi, M. C.; Rizzi, G. A.; Isse, A. A.; Durante, C.; Gennaro, A. Mesoporous Carbon with Different Density of Thiophenic-Like Functional Groups and Their Effect on Oxygen Reduction. *ChemSusChem* **2019**, *12*, 4229–4239, doi:10.1002/cssc.201901568.
11. Brandiele, R.; Durante, C.; Zerbetto, M.; Vicentini, N.; Kosmala, T.; Badocco, D.; Pastore, P.; Rizzi, G. A.; Isse, A. A.; Gennaro, A. Probing the correlation between Pt-support interaction and oxygen reduction reaction activity in mesoporous carbon materials modified with Pt-N active sites. *Electrochim. Acta* **2018**, *277*, 287–300, doi:10.1016/j.electacta.2018.04.182.
12. Perazzolo, V.; Brandiele, R.; Durante, C.; Zerbetto, M.; Causin, V.; Rizzi, G. A.; Cerri, I.; Granozzi, G.; Gennaro, A. Density Functional Theory (DFT) and Experimental Evidences of Metal–Support Interaction in Platinum Nanoparticles Supported on Nitrogen- and Sulfur-Doped Mesoporous Carbons: Synthesis, Activity, and Stability. *ACS Catal.* **2018**, *8*, 1122–1137, doi:10.1021/acscatal.7b03942.
13. Primbs, M.; Sun, Y.; Roy, A.; Malko, D.; Mehmood, A.; Sougrati, M.-T.; Blanchard, P.-Y.; Granozzi, G.; Kosmala, T.; Daniel, G.; Atanassov, P.; Sharman, J.; Durante, C.; Kucernak, A.; Jones, D. J.; Jaouen, F.; Strasser, P. Establishing Reactivity Descriptors for Platinum Group Metal (PGM)-free Fe-N-C Catalysts for PEM Fuel Cells. *Energy Environ. Sci.* **2020**, *10*, 147–154, doi:10.1039/D0EE01013H.
14. Jaouen, F.; Herranz, J.; Lefèvre, M.; Dodelet, J.-P.; Kramm, U. I.; Herrmann, I.; Bogdanoff, P.; Maruyama, J.; Nagaoka, T.; Garsuch, A.; Dahn, J. R.; Olson, T.; Pylypenko, S.; Atanassov, P.; Ustinov, E. A. Cross-Laboratory Experimental Study of Non-Noble-Metal Electrocatalysts for the Oxygen Reduction Reaction. *ACS Appl. Mater. Interfaces* **2009**, *1*, 1623–1639, doi:10.1021/am900219g.
15. Mineva, T.; Matanovic, I.; Atanassov, P.; Sougrati, M.-T.; Stievano, L.; Clémancey, M.; Kochem, A.; Latour, J.-M.; Jaouen, F. Understanding Active Sites in Pyrolyzed Fe–N–C Catalysts for Fuel Cell Cathodes by Bridging Density Functional Theory Calculations and 57 Fe Mössbauer Spectroscopy. *ACS Catal.* **2019**, *9*, 9359–9371, doi:10.1021/acscatal.9b02586.
16. Shao, Y.; Dodelet, J.; Wu, G.; Zelenay, P. PGM-Free Cathode Catalysts for PEM Fuel Cells: A Mini-Review on Stability Challenges. *Adv. Mater.* **2019**, *31*, 1807615, doi:10.1002/adma.201807615.
17. Martinez, U.; Komini Babu, S.; Holby, E. F.; Zelenay, P. Durability challenges and perspective in the development of PGM-free electrocatalysts for the oxygen reduction reaction. *Curr. Opin. Electrochem.* **2018**, *9*, 224–232, doi:10.1016/j.coelec.2018.04.010.
18. Martinaiou, I.; Shahraei, A.; Grimm, F.; Zhang, H.; Wittich, C.; Klemenz, S.; Dolique, S. J.; Kleebe, H.-J.; Stark, R. W.; Kramm,

U. I. Effect of metal species on the stability of Me-N-C catalysts during accelerated stress tests mimicking the start-up and shut-down conditions. *Electrochim. Acta* **2017**, *243*, 183–196, doi:10.1016/j.electacta.2017.04.134.

19. Primbs, M.; Sun, Y.; Roy, A.; Malko, D.; Mehmood, A.; Sougrati, M.-T.; Blanchard, P.-Y.; Granozzi, G.; Kosmala, T.; Daniel, G.; Atanassov, P.; Sharman, J.; Durante, C.; Kucernak, A.; Jones, D.; Jaouen, F.; Strasser, P. Establishing reactivity descriptors for platinum group metal (PGM)-free Fe–N–C catalysts for PEM fuel cells. *Energy Environ. Sci.* **2020**, *13*, 2480–2500, doi:10.1039/D0EE01013H.
20. Mazzucato Marco; Giorgia, D.; Tomasz, K.; Mahmood, A.; Gaetano, G.; Anthony, K.; Durante, C. Effects of the induced Micro- and Meso-porosity on the single site density and turn over frequency of Fe-N-C carbon electrodes for the Oxygen Reduction Reaction. *Appl. Catal. B Environ.* **2021**, accepted.
21. Mineva, T.; Matanovic, I.; Atanassov, P.; Sougrati, M.-T.; Stievano, L.; Clémancey, M.; Kochem, A.; Latour, J.-M.; Jaouen, F. Understanding Active Sites in Pyrolyzed Fe–N–C Catalysts for Fuel Cell Cathodes by Bridging Density Functional Theory Calculations and 57 Fe Mössbauer Spectroscopy. *ACS Catal.* **2019**, *9*, 9359–9371, doi:10.1021/acscatal.9b02586.
22. Lai, Y.; Wang, Q.; Wang, M.; Li, J.; Fang, J.; Zhang, Z. Facile synthesis of mesoporous Fe-N-C electrocatalyst for high performance alkaline aluminum-air battery. *J. Electroanal. Chem.* **2017**, *801*, 72–76, doi:10.1016/j.jelechem.2017.07.034.
23. Zhang, X.; Han, X.; Jiang, Z.; Xu, J.; Chen, L.; Xue, Y.; Nie, A.; Xie, Z.; Kuang, Q.; Zheng, L. Atomically dispersed hierarchically ordered porous Fe–N–C electrocatalyst for high performance electrocatalytic oxygen reduction in Zn-Air battery. *Nano Energy* **2020**, *71*, 104547–104556, doi:10.1016/j.nanoen.2020.104547.
24. Meng, Z.; Stolz, R. M.; Mendecki, L.; Mirica, K. A. Electrically-Transduced Chemical Sensors Based on Two-Dimensional Nanomaterials. *Chem. Rev.* **2019**, *119*, 478–598, doi:10.1021/acs.chemrev.8b00311.
25. Paolesse, R.; Nardis, S.; Monti, D.; Stefanelli, M.; Di Natale, C. Porphyrinoids for Chemical Sensor Applications. *Chem. Rev.* **2017**, *117*, 2517–2583, doi:10.1021/acs.chemrev.6b00361.
26. Wang, D.; Hu, J.; Yang, J.; Xiao, K.; Liang, S.; Xu, J.; Liu, B.; Hou, H. Fe and N co-doped carbon derived from melamine resin capsuled biomass as efficient oxygen reduction catalyst for air-cathode microbial fuel cells. *Int. J. Hydrogen Energy* **2020**, *45*, 3163–3175, doi:10.1016/j.ijhydene.2019.11.201.
27. Daniel, G.; Foltran, E.; Brandiele, R.; Nodari, L.; Pilot, R.; Menna, E.; Rizzi, G. A.; Isse, A. A.; Durante, C.; Gennaro, A. Platinum-free electrocatalysts for oxygen reduction reaction: Fe-Nx modified mesoporous carbon prepared from biosources. *J. Power Sources* **2018**, *402*, 434–446, doi:10.1016/j.jpowsour.2018.09.060.
28. Artyushkova, K.; Serov, A.; Rojas-Carbonell, S.; Atanassov, P. Chemistry of Multitudinous Active Sites for Oxygen Reduction Reaction in Transition Metal–Nitrogen–Carbon Electrocatalysts. *J. Phys. Chem. C* **2015**, *119*, 25917–25928, doi:10.1021/acs.jpcc.5b07653.
29. Matanovic, I.; Artyushkova, K.; Atanassov, P. Understanding PGM-free catalysts by linking density functional theory calculations and structural analysis: Perspectives and challenges. *Curr. Opin. Electrochem.* **2018**, *9*, 137–144, doi:10.1016/j.coelec.2018.03.009.
30. Matanovic, I.; Artyushkova, K.; Strand, M. B.; Dzara, M. J.; Pylypenko, S.; Atanassov, P. Core Level Shifts of Hydrogenated Pyridinic and Pyrrolic Nitrogen in the Nitrogen-Containing Graphene-Based Electrocatalysts: In-Plane vs Edge Defects. *J. Phys. Chem. C* **2016**, *120*, 29225–29232, doi:10.1021/acs.jpcc.6b09778.
31. Li, J.; Sougrati, M. T.; Zitolo, A.; Ablett, J. M.; Oğuz, I. C.; Mineva, T.; Matanovic, I.; Atanassov, P.; Huang, Y.; Zenyuk, I.; Di Cicco, A.; Kumar, K.; Dubau, L.; Maillard, F.; Dražić, G.; Jaouen, F. Identification of durable and non-durable FeNx sites in Fe–N–C materials for proton exchange membrane fuel cells. *Nat. Catal.* **2021**, *4*, 10–19, doi:10.1038/s41929-020-00545-2.
32. Yang, W.; Wang, X.; Rossi, R.; Logan, B. E. Low-cost Fe–N–C catalyst derived from Fe (III)-chitosan hydrogel to enhance power production in microbial fuel cells. *Chem. Eng. J.* **2020**, *380*, 122522, doi:10.1016/j.cej.2019.122522.
33. Chenitz, R.; Kramm, U. I.; Lefèvre, M.; Glibin, V.; Zhang, G.; Sun, S.; Dodelet, J.-P. A specific demetalation of Fe–N_4 catalytic sites in the micropores of NC_Ar + NH_3 is at the origin of the initial activity loss of the highly active Fe/N/C catalyst used for the reduction of oxygen in PEM fuel cells. *Energy Environ. Sci.* **2018**, *11*, 365–382, doi:10.1039/C7EE02302B.

34. Jaouen, F.; Lefèvre, M.; Dodelet, J.-P.; Cai, M. Heat-Treated Fe/N/C Catalysts for O_2 Electroreduction: Are Active Sites Hosted in Micropores? *J. Phys. Chem. B* **2006**, *110*, 5553–5558, doi:10.1021/jp057135h.
35. Liang, C.; Li, Z.; Dai, S. Mesoporous Carbon Materials: Synthesis and Modification. *Angew. Chemie Int. Ed.* **2008**, *47*, 3696–3717, doi:10.1002/anie.200702046.
36. Asset, T.; Atanassov, P. Iron-Nitrogen-Carbon Catalysts for Proton Exchange Membrane Fuel Cells. *Joule* **2020**, *4*, 33–44, doi:10.1016/j.joule.2019.12.002.
37. Perazzolo, V.; Durante, C.; Pilot, R.; Paduano, A.; Zheng, J.; Rizzi, G. A.; Martucci, A.; Granozzi, G.; Gennaro, A. Nitrogen and sulfur doped mesoporous carbon as metal-free electrocatalysts for the in situ production of hydrogen peroxide. *Carbon* **2015**, *95*, 949–963, doi:10.1016/j.carbon.2015.09.002.
38. Perazzolo, V.; Durante, C.; Gennaro, A. Nitrogen and sulfur doped mesoporous carbon cathodes for water treatment. *J. Electroanal. Chem.* **2016**, *782*, 264–269, doi:10.1016/j.jelechem.2016.10.037.
39. Perazzolo, V.; Grądzka, E.; Durante, C.; Pilot, R.; Vicentini, N.; Rizzi, G. A.; Granozzi, G.; Gennaro, A. Chemical and electrochemical stability of nitrogen and sulphur doped mesoporous carbons. *Electrochim. Acta* **2016**, *197*, 251–262, doi:10.1016/j.electacta.2016.02.025.
40. Brandiele, R.; Picelli, L.; Pilot, R.; Causin, V.; Martucci, A.; Rizzi, G. A.; Isse, A. A.; Durante, C.; Gennaro, A. Nitrogen and Sulfur Doped Mesoporous Carbons, Prepared from Templating Silica, as Interesting Material for Supercapacitors. *ChemistrySelect* **2017**, *2*, 7082–7090, doi:10.1002/slct.201701404.
41. Brandiele, R.; Poli, F.; Picelli, L.; Pilot, R.; Rizzi, G. A.; Soavi, F.; Durante, C. Nitrogen doped mesoporous carbon electrodes prepared from templating propylamine functionalized silica. *ChemElectroChem* **2020**, *92*, 455–459, doi:10.1002/celc.202000098.
42. Perazzolo, V.; Daniel, G.; Brandiele, R.; Picelli, L.; Rizzi, G. A.; Isse, A. A.; Durante, C. PEO-b-PS Block Copolymer Templated Mesoporous Carbons: A Comparative Study of Nitrogen and Sulfur Doping in the Oxygen Reduction Reaction to Hydrogen Peroxide. *Chem. – A Eur. J.* **2021**, *27*, 1002–1014, doi:10.1002/chem.202003355.
43. Trevisanello, E.; De Bon, F.; Daniel, G.; Lorandi, F.; Durante, C.; Isse, A. A.; Gennaro, A. Electrochemically mediated atom transfer radical polymerization of acrylonitrile and poly(acrylonitrile-b-butyl acrylate) copolymer as a precursor for N-doped mesoporous carbons. *Electrochim. Acta* **2018**, *285*, 344–354, doi:10.1016/j.electacta.2018.07.209.
44. Daniel, G.; Kosmala, T.; Dalconi, M. C.; Nodari, L.; Badocco, D.; Pastore, P.; Lorenzetti, A.; Granozzi, G.; Durante, C. Upcycling of polyurethane into iron-nitrogen-carbon electrocatalysts active for oxygen reduction reaction. *Electrochim. Acta* **2020**, *362*, 137200, doi:10.1016/j.electacta.2020.137200.
45. Huang, R.; Lei, Y.; Zhang, D.; Xie, H.; Liu, X.; Wang, H. Solvent-Free Assembled Fe-Chitosan Chelates Derived N-Doped Carbon Layer-Encapsulated Fe/Fe 3 C for ORR and OER. *Nano* **2020**, *15*, 2050070, doi:10.1142/S1793292020500708.
46. Wang, W.; Liu, S.; Liu, Y.; Jing, W.; Zhao, R.; Lei, Z. Phenolic resin/chitosan composite derived nitrogen-doped carbon as highly durable and anti-poisoning electrocatalyst for oxygen reduction reaction. *Int. J. Hydrogen Energy* **2017**, *42*, 26704–26712, doi:10.1016/j.ijhydene.2017.09.024.
47. Aghabarari, B.; Martínez-Huerta, M. V.; Capel-Sánchez, M. C.; Lázaro, M. J. Non-precious Melamine/Chitosan Composites for the Oxygen Reduction Reaction: Effect of the Transition Metal. *Front. Mater.* **2020**, *7*, 1–9, doi:10.3389/fmats.2020.578518.
48. Khan, A.; Goepel, M.; Colmenares, J. C.; Gläser, R. Chitosan-Based N-Doped Carbon Materials for Electrocatalytic and Photocatalytic Applications. *ACS Sustain. Chem. Eng.* **2020**, *8*, 4708–4727, doi:10.1021/acssuschemeng.9b07522.
49. Borghei, M.; Lehtonen, J.; Liu, L.; Rojas, O. J. Advanced Biomass-Derived Electrocatalysts for the Oxygen Reduction Reaction. *Adv. Mater.* **2018**, *30*, 1703691, doi:10.1002/adma.201703691.
50. Zhang, B.; Wang, C.; Liu, D.; Liu, Y.; Yu, X.; Wang, L. Boosting ORR Electrocatalytic Performance of Metal-Free Mesoporous Biomass Carbon by Synergism of Huge Specific Surface Area and Ultrahigh Pyridinic Nitrogen Doping. *ACS Sustain. Chem. Eng.* **2018**, *6*, 13807–13812, doi:10.1021/acssuschemeng.8b01876.
51. Daniel, G.; Zhang, Y.; Lanzalaco, S.; Brombin, F.; Kosmala, T.; Granozzi, G.; Wang, A.; Brillas, E.; Sirés, I.; Durante, C. Chitosan-Derived Nitrogen-Doped Carbon Electrocatalyst for a Sustainable Upgrade of Oxygen Reduction to Hydrogen

Peroxide in UV-Assisted Electro-Fenton Water Treatment. *ACS Sustain. Chem. Eng.* **2020**, *8*, 14425–14440, doi:10.1021/acssuschemeng.0c04294.

52. Zhang, G.; Li, L.; Chen, M.; Yang, F. Chitosan cross-linked poly(aminoanthraquinone)/Prussian blue ternary nitrogen precursor-derived Fe–N–C oxygen reduction catalysts for microbial fuel cells and zinc–air batteries. *J. Mater. Chem. A* **2020**, *8*, 9256–9267, doi:10.1039/D0TA00306A.
53. Schmitz, C.; Auza, L. G.; Koberidze, D.; Rasche, S.; Fischer, R.; Bortesi, L. Conversion of chitin to defined chitosan oligomers: Current status and future prospects. *Mar. Drugs* **2019**, *17*, 1–22, doi:10.3390/md17080452.
54. Zhong, H.; Duan, L.; Ye, P.; Li, X.; Xu, A.; Peng, Q. Synthesis of cobalt–nitrogen-doped mesoporous carbon from chitosan and its performance for pollutant degradation as Fenton-like catalysts. *Res. Chem. Intermed.* **2019**, *45*, 907–918, doi:10.1007/s11164-018-3655-y.
55. Nie, J.; Wang, Z.; Hu, Q. Difference between Chitosan Hydrogels via Alkaline and Acidic Solvent Systems. *Sci. Rep.* **2016**, *6*, 36053, doi:10.1038/srep36053.
56. Tong, X.; Chen, Z.; Zhuo, H.; Hu, Y.; Jing, S.; Liu, J.; Zhong, L. Tailoring the physicochemical properties of chitosan-derived N-doped carbon by controlling hydrothermal carbonization time for high-performance supercapacitor application. *Carbohydr. Polym.* **2019**, *207*, 764–774, doi:10.1016/j.carbpol.2018.12.048.
57. Jurca, B.; Bucur, C.; Primo, A.; Concepción, P.; Parvulescu, V. I.; García, H. N-Doped Defective Graphene from Biomass as Catalyst for CO2 Hydrogenation to Methane. *ChemCatChem* **2019**, *11*, 985–990, doi:10.1002/cctc.201801984.
58. Liao, C.; Liu, B.; Chi, Q.; Zhang, Z. Nitrogen-Doped Carbon Materials for the Metal-Free Reduction of Nitro Compounds. *ACS Appl. Mater. Interfaces* **2018**, *10*, 44421–44429, doi:10.1021/acsami.8b15300.
59. Conder, J.; Vaulot, C.; Marino, C.; Villevieille, C.; Ghimbeu, C. Chitin and chitosan – structurally-related precursors of dissimilar hard carbons for Na-ion battery. *ACS Appl. Energy Mater.* **2019**, *2*, 4841–4852.
60. Qiao, Y.; Kong, F.; Zhang, C.; Li, R.; Kong, A.; Shan, Y. Highly efficient oxygen electrode catalyst derived from chitosan biomass by molten salt pyrolysis for zinc-air battery. *Electrochim. Acta* **2020**, *339*, doi:10.1016/j.electacta.2020.135923.
61. Li, Y.; Liu, T.; Yang, W.; Zhu, Z.; Zhai, Y.; Gu, W.; Zhu, C. Multiscale porous Fe-N-C networks as highly efficient catalysts for the oxygen reduction reaction. *Nanoscale* **2019**, *11*, 19506–19511, doi:10.1039/c9nr05726a.
62. Zhang, Y.; Lu, L.; Zhang, S.; Lv, Z.; Yang, D.; Liu, J.; Chen, Y.; Tian, X.; Jin, H.; Song, W. Biomass chitosan derived cobalt/nitrogen doped carbon nanotubes for the electrocatalytic oxygen reduction reaction. *J. Mater. Chem. A* **2018**, *6*, 5740–5745, doi:10.1039/C7TA11258K.
63. Wang, Y.; Li, B.; Zhou, Y.; Jia, D.; Song, Y. CS-Fe(II,III) complex as precursor for magnetite nanocrystal. *Polym. Adv. Technol.* **2011**, *22*, 1681–1684, doi:10.1002/pat.1657.
64. Thommes, M.; Kaneko, K.; Neimark, A. V; Olivier, J. P.; Rodriguez-Reinoso, F.; Rouquerol, J.; Sing, K. S. W. Physisorption of gases, with special reference to the evaluation of surface area and pore size distribution (IUPAC Technical Report). *Pure Appl. Chem.* **2015**, *87*, 1051–1069, doi:10.1515/pac-2014-1117.
65. Poddubnaya, A. M. P. O. I.; Sobiesiak, B. G. M. Comparison of heterogeneous pore models QSDFT and 2D-NLDFT and computer programs ASiQwin and SAIEUS for calculation of pore size distribution. **2016**, 459–464, doi:10.1007/s10450-015-9704-6.
66. PÃ©rez-RamÃ-rez, J.; Verboekend, D.; Bonilla, A.; AbellÃ³, S. Zeolite Catalysts with Tunable Hierarchy Factor by Pore-Growth Moderators. *Adv. Funct. Mater.* **2009**, *19*, 3972–3979, doi:10.1002/adfm.200901394.
67. Ferrari, A. C.; Robertson, J. Interpretation of Raman spectra of disordered and amorphous carbon. *Phys. Rev. B* **2000**, *61*, 14095–14107, doi:10.1103/PhysRevB.61.14095.
68. Sadezky, A.; Muckenhuber, H.; Grothe, H.; Niessner, R.; Pöschl, U. Raman microspectroscopy of soot and related carbonaceous materials: Spectral analysis and structural information. *Carbon* **2005**, *43*, 1731–1742, doi:10.1016/j.carbon.2005.02.018.
69. Pawlyta, M.; Rouzaud, J.-N.; Duber, S. Raman microspectroscopy characterization of carbon blacks: Spectral analysis and

structural information. *Carbon* **2015**, *84*, 479–490, doi:10.1016/j.carbon.2014.12.030.

70. Beyssac, O.; Goffé, B.; Petitet, J.-P.; Froigneux, E.; Moreau, M.; Rouzaud, J.-N. On the characterization of disordered and heterogeneous carbonaceous materials by Raman spectroscopy. *Spectrochim. Acta Part A Mol. Biomol. Spectrosc.* **2003**, *59*, 2267–2276, doi:10.1016/S1386-1425(03)00070-2.
71. Malko, D.; Kucernak, A.; Lopes, T. Performance of Fe–N/C Oxygen Reduction Electrocatalysts toward NO_2^- , NO, and NH_2OH Electroreduction: From Fundamental Insights into the Active Center to a New Method for Environmental Nitrite Destruction. *J. Am. Chem. Soc.* **2016**, *138*, 16056–16068, doi:10.1021/jacs.6b09622.
72. Malko, D.; Kucernak, A.; Lopes, T. In situ electrochemical quantification of active sites in Fe–N/C non-precious metal catalysts. *Nat. Commun.* **2016**, *7*, 13285–13292, doi:10.1038/ncomms13285.